ChemSusChem

Supporting Information

Development of a Mg/O ReaxFF Potential to describe the Passivation Processes in Magnesium-Ion Batteries**

Florian Fiesinger, Daniel Gaissmaier, Matthias van den Borg, Julian Beßner, Adri C. T. van Duin, and Timo Jacob*This publication is part of a collection of papers from contributors to the 7th Ertl Symposium on Catalysis in Electrochemistry (Gwangju, South Korea, October 26–29, 2022). Please visit to view all contributions.

Mg/O force field file

```
Reactive MD-force field: F. Fiesinger (2022) - Mg/O FF
 39          ! Number of general parameters
   50.0000 !p_boc1 Eq(4c): Overcoordination parame
    9.5469 !p_boc2 Eq(4d): Overcoordination parame
   26.5405 !p_coa2 Eq(15): Valency angle conjugati
    1.7224 !p_trip4 Eq(20): Triple bond stabilisat
    6.8702 !p_trip3 Eq(20): Triple bond stabilisat
   60.4850 !k_c2 Eq(19): C2-correction
    1.0588 !p_ovun6 Eq(12): Undercoordination
    4.6000 !p_trip2 Eq(20): Triple bond stabilisat
   12.1176 !p_ovun7 Eq(12): Undercoordination
   13.3056 !p_ovun8 Eq(12): Undercoordination
  -30.5044 !p_trip1 Eq(20): Triple bond stabilizat
    0.0000 !Lower Taper-radius (must be 0)
   10.0000 !R_cut Eq(21): Upper Taper-radius
    2.8793 !p_fe1 Eq(6a): Fe dimer correction
   15.0000 !p_val6 Eq(13c): Valency undercoordinat
    6.0891 !p_lp1 Eq(8): Lone pair param
    1.0563 !p_val9 Eq(13f): Valency angle exponent
    2.0384 !p_val10 Eq(13g): Valency angle paramet
    6.1431 !p_fe2 Eq(6a): Fe dimer correction
    6.9290 !p_pen2 Eq(14a): Double bond/angle para
    0.3989 !p_pen3 Eq(14a): Double bond/angle para
    3.9954 !p_pen4 Eq(14a): Double bond/angle para
   -2.4837 !p_fe3 Eq(6a): Fe dimer correction
    5.7796 !p_tor2 Eq(16b): Torsion/BO parameter
   10.0000 !p_tor3 Eq(16c): Torsion overcoordinati
    1.9487 !p_tor4 Eq(16c): Torsion overcoordinati
   -1.2327 !p_elho Eq(26a): electron-hole interact
    2.1645 !p_cot2 Eq(17b): Conjugation if tors13=
    1.5591 !p_vdW1 Eq(23b): vdWaals shielding
    0.0010 !Cutoff for bond order (*100)
    2.1365 !p_coa4 Eq(15): Valency angle conjugati
    0.6991 !p_ovun4 Eq(11b): Over/Undercoordinatio
   50.0000 !p_ovun3 Eq(11b): Over/Undercoordinatio
    1.8512 !p_val8 Eq(13d): Valency/lone pair para
    0.5000 !X_soft Eq(25): ACKS2 softness for X_ij
   20.0000 !d Eq(23d): Scale factor in lg-dispersi
    5.0000 !p_val Eq(27): Gauss exponent for elect
    0.0000 !l Eq(13e): disable undecoord in val an
    2.6962 !p_coa3 Eq(15): Valency angle conjugati
  2     ! Nr of atoms; cov.r; valency;a.m;Rvdw;Evdw;gammaEEM;cov.r2;#
            alfa;gammavdW;valency;Eunder;Eover;chiEEM;etaEEM;n.u.
            cov r3;Elp;Heat inc.;bo131;bo132;bo133;softcut;n.u.
            ov/un;val1;n.u.;val3,vval4
O     1.2450    2.0000   15.9990    2.3890    0.1000    1.0898    1.0548    6.0000
      9.7300   13.8449    4.0000   37.5000  116.0768    8.5000    8.3122    2.0000
      0.9049    0.4056   59.0626    3.5027    0.7640    0.0021    0.9745    0.0000
     -3.5500    2.9000    1.0493    4.0000    2.9225    1.3000    0.2000   13.0000
Mg    1.8315    2.0000   24.3050    2.2464    0.1806    0.7404    1.0000    2.0000
     10.9186   27.1205    3.0000   38.0000    0.0000    0.6422    5.4853    0.0000
     -1.3000    0.0000  220.0000   49.9248    0.3370    0.0000    0.0000    0.0000
     -2.5000    2.3663    1.0564    6.0000    2.9663    2.4500    1.0000   40.0000
  3     ! Nr of bonds; Edis1;LPpen;n.u.;pbe1;pbo5;13corr;pbo6
                       pbe2;pbo3;pbo4;n.u.;pbo1;pbo2;ovcorr
  1  1 142.2858  145.0000   50.8293    0.2506   -0.1000    1.0000   29.7503    0.6051
        0.3451   -0.1055    9.0000    1.0000   -0.1225    5.5000    1.0000    0.0000
  1  2  53.7362    0.0000   43.3991    0.4817   -0.3000    1.0000   36.0000    0.0667
        0.4678   -0.2000    8.4994    1.0000   -0.1486    8.8494    1.0000   24.4461
  2  2  25.1797    0.0000    0.0000    0.6249   -0.2050    0.0000   16.0000    0.2618
        0.7684   -0.2000   10.0000    1.0000   -0.2374    3.2858    0.0000    0.0000
  1     ! Nr of off-diagonal terms; Ediss;Ro;gamma;rsigma;rpi;rpi2
  1  2   1.0196    1.1711   13.4732    1.9128   -1.0000   -1.0000
  5     ! Nr of angles;at1;at2;at3;Thetao,o;ka;kb;pv1;pv2
```

```
1   1   1   80.7324   30.4554    0.9953    0.0000    1.6310   50.0000    1.0783
1   2   1    0.0000   21.1509    1.9901    0.0000    1.0311    0.0000    2.2855
2   1   2   90.0000    5.7293    0.5286    0.0000    1.6966    0.0000    1.3853
1   1   2   16.1468    4.6234    1.5549    0.0000    1.0488    0.0000    1.0830
1   2   2   21.8146    6.1011    0.5672    0.0000    2.1986    0.0000    1.5074
3     ! Nr of torsions;at1;at2;at3;at4;;V1;V2;V3;V2(BO);vconj;n.u;n
1   1   1   1   -2.5000    0.0100    1.0000   -9.0000   -0.0100    0.0000    0.0000
0   1   1   0    0.5511   25.4150    1.1330   -5.1903   -1.0000    0.0000    0.0000
2   1   1   2    0.4381   23.9911    1.2283   -5.1903   -1.0000    0.0000    0.0000
0     ! Nr of hydrogen bonds;at1;at2;at3;Rhb;Dehb;vhb1
```

Computational details

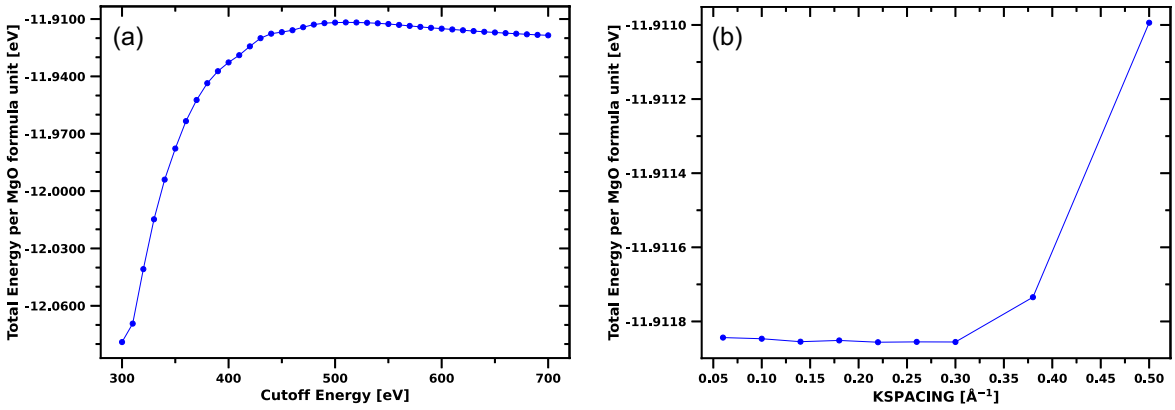

Figure S1: Convergence studies of the a) cutoff energy (ENCUT Tag) and b) grid density of k-points (KSPACING Tag) for the MgO bulk structure.

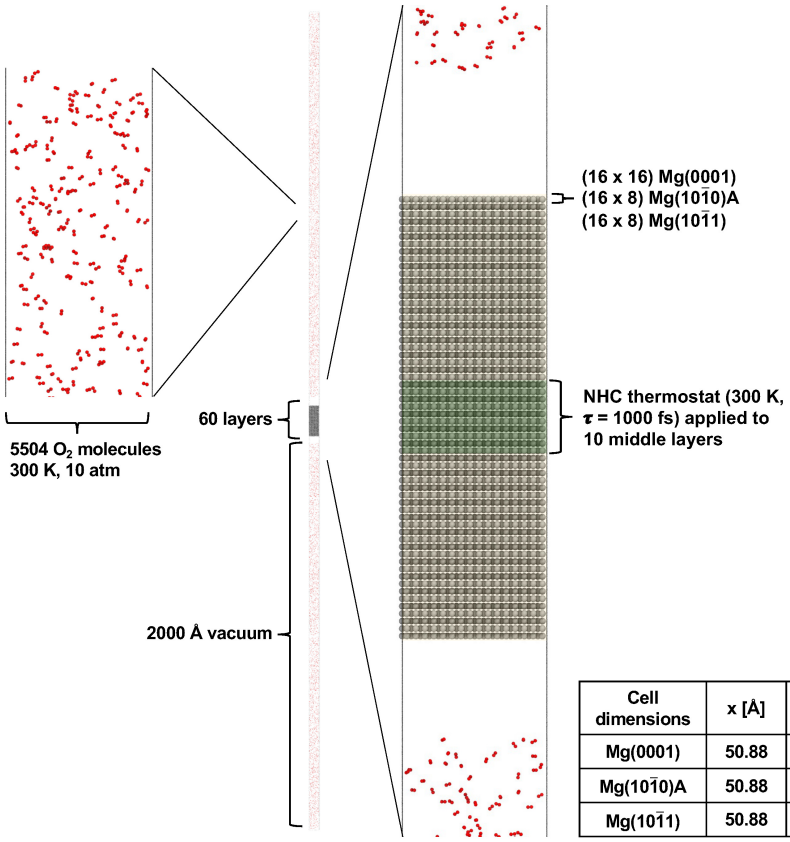

Cell dimensions	x [Å]	y [Å]	z [Å]
Mg(0001)	50.88	44.06	4153.40
Mg(10$\bar{1}$0)A	50.88	41.60	4167.07
Mg(10$\bar{1}$1)	50.88	47.07	4148.05

Figure S2: Cell dimensions and simulation settings used to model passivation of the magnesium anode.

Mg adsorption on Mg(0001), Mg$(10\bar{1}0)$A, and Mg$(10\bar{1}1)$

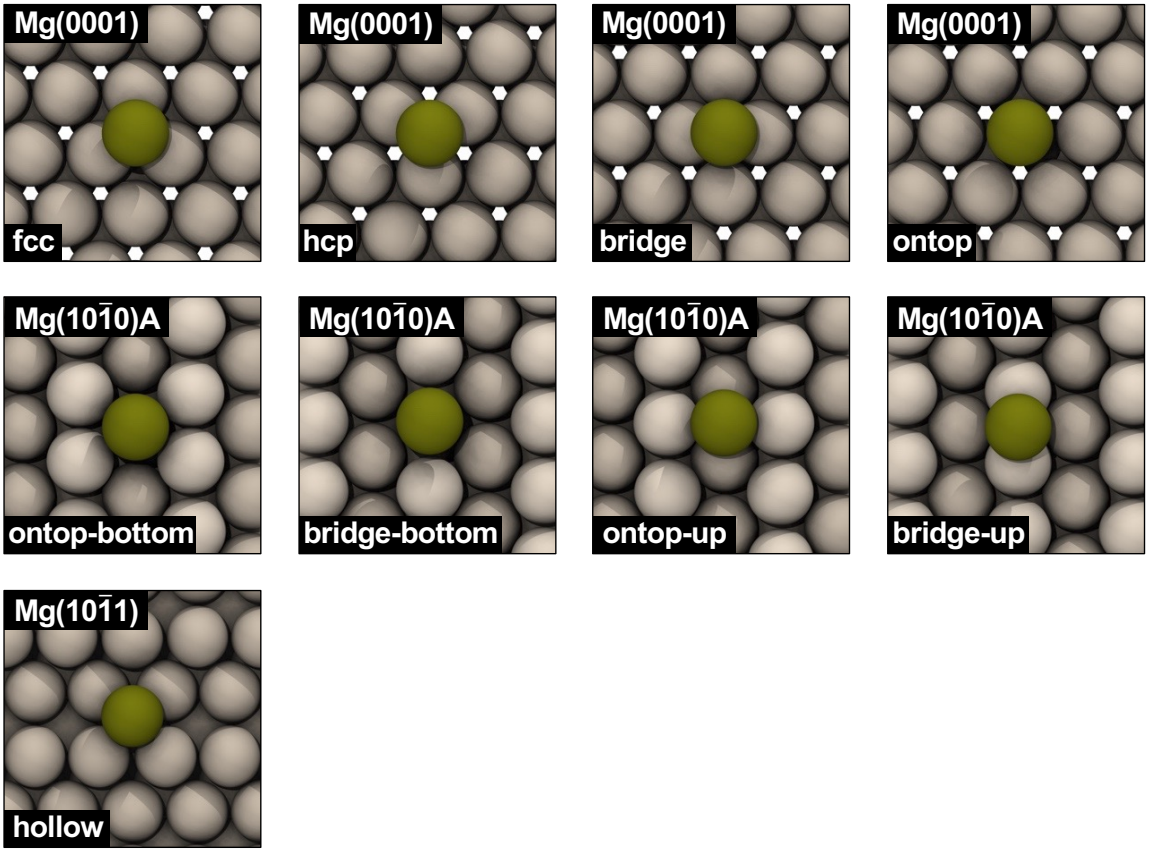

Figure S3: Schematic illustration of Mg adsorption sites on Mg(0001), Mg$(10\bar{1}0)$A, and Mg$(10\bar{1}1)$. The green-colored atom is the magnesium adsorbate, and the gray-colored atoms are surface atoms. Adapted from Ref. [1] Copyright (2022), with permission from Wiley-VCH.

Mg diffusion processes on Mg(0001)

A detailed comparison of the activation energy results calculated with ReaxFF and DFT is provided in Table S1. We previously showed that Mg dimer formation on Mg(0001) occurs barrier-free and that its cleavage is associated with a barrier that is several times larger (Figure S4a and S4b).[1] The trained ReaxFF force field reproduces this trend only qualitatively: the barriers for dimer formation are shallow (0.11 eV and 0.12 eV) but so are the reverse barriers (0.28 eV and 0.29 eV). A similar overestimation occurs for the diffusion of a Mg atom towards a $[11\overline{2}0]$-directed step-edge (0.22 eV *vs.* 0.03 eV; Figure S4c) but diffusion along the step-edge is accurately reproduced (both 0.22 eV; Figure S4c and S4d). The trained ReaxFF force field describes the kink processes well (Figure S4e and S4f), both when the atom leaves the site towards the terrace (0.72 eV *vs.* 0.91 eV/ 0.92 eV) and along the step-edge (0.44 eV/ 0.47 eV *vs.* 0.45 eV/ 0.46 eV). Analogous to the dimer systems, the force field underestimates the barriers for bond breaking (0.43 eV/ 0.46 eV *vs.* 0.63 eV/ 0.62 eV) for inner-corner processes (Figure S4g and S4h) but overestimates bond formation barriers (0.21 eV/ 0.25 eV *vs.* 0.10 eV/ 0.08 eV). Precisely as in DFT, the exchange process at a 240° outer-corner (Figure S4k) exhibits a higher barrier than diffusion around the corner with the trained force field. However, unlike in the DFT reference data set, the OC_1 site is thermodynamically more stable than the OC_0 site. Furthermore, with the force field, the exchange processes are much better reproduced at the 300° outer-corners (Figure S4i and S4j) than at the terrace, even though the barriers are still slightly overestimated. Finally, DFT predicts an almost barrier-free descent via the exchange process on $[11\overline{2}0]$- and $[\overline{11}20]$-steps (0.01 eV/ 0.02 eV; Figure S4l and S4m).[1] Because the force field overestimates the exchange processes in general, the barriers to descent are generally higher (0.27 eV/ 0.13 eV). The activation barriers for the ascent, on the other hand, are well reproduced for hopping and exchange processes ($\Delta|E_a| \leq 0.1$ eV).

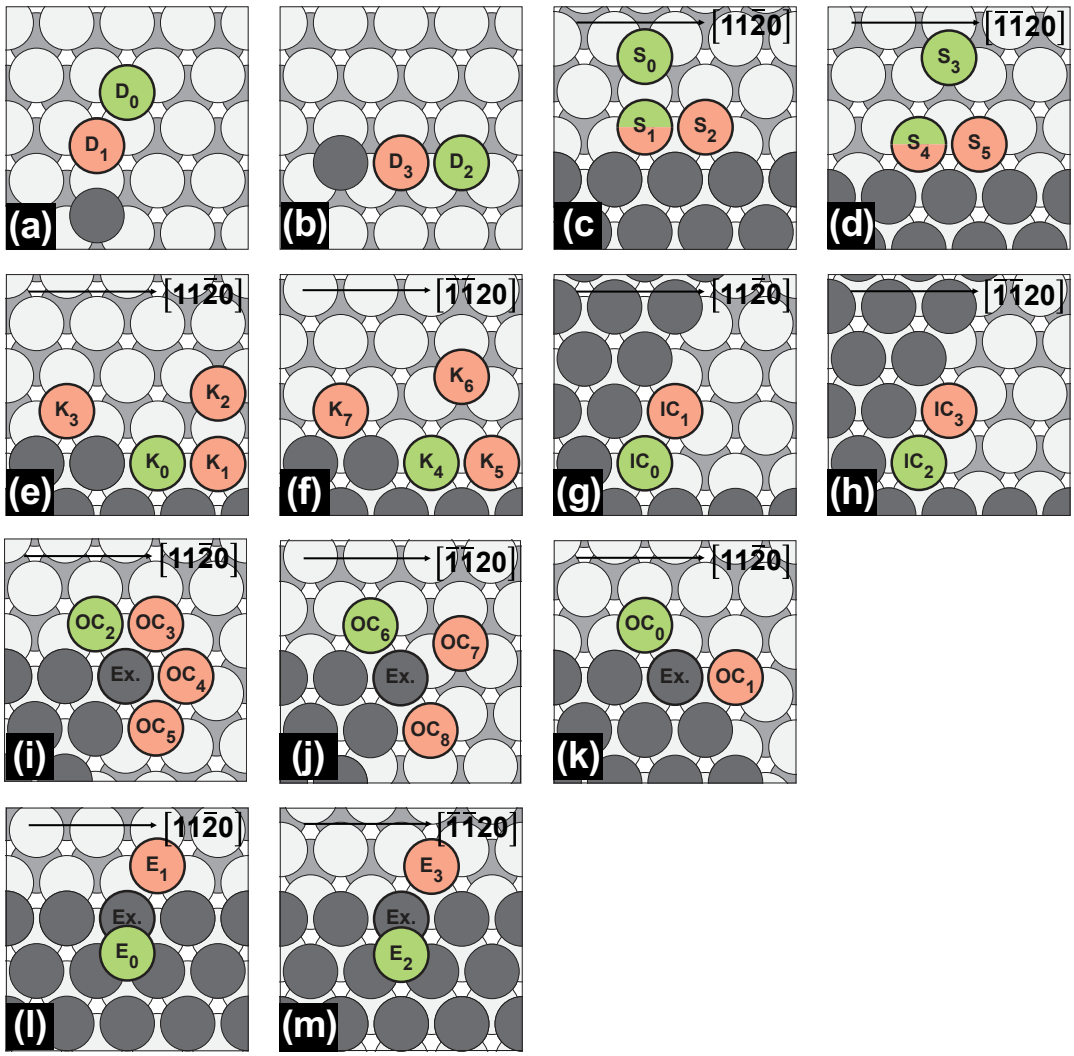

Figure S4: Overview and schematic representation of trained self-diffusion processes on Mg(0001): a) dimer I, b) dimer II, c) step-edge [11$\bar{2}$0]-step, d) step-edge [$\bar{1}\bar{1}$20]-step, e) kink [11$\bar{2}$0]-step, f) kink [$\bar{1}\bar{1}$20]-step, g) 60° inner-corner [11$\bar{2}$0]-step, h) 60° inner-corner [$\bar{1}\bar{1}$20]-step, i) 300° outer-corner [11$\bar{2}$0]-step, j) 300° outer-corner [$\bar{1}\bar{1}$20]-step k) 240° outer-corner, l) step-down [11$\bar{2}$0]-step, m) step-down [$\bar{1}\bar{1}$20]-step. Green atoms mark the initial, while red atoms mark the final position. Adapted from Ref. [1] Copyright (2022), with permission from Wiley-VCH.

Table S1: Comparison of activation energies E_a in eV calculated with ReaxFF and DFT using Equation (8) for forward and backward self-diffusion processes on Mg(0001). DFT reference activation energy values were adopted from Fiesinger et al.[1]

Mg(0001)	Pathway	$E_{a,ReaxFF}^{for}$	$E_{a,DFT}^{for}$	$\lvert\Delta E_a^{for}\rvert$	$E_{a,ReaxFF}^{rev}$	$E_{a,DFT}^{rev}$	$\lvert\Delta E_a^{rev}\rvert$
dimer	$D_0 \leftrightarrow D_1$	0.11	0.00	0.11	0.28	0.49	0.21
	$D_2 \leftrightarrow D_3$	0.12	0.00	0.12	0.29	0.46	0.17
step-edge	$S_0 \leftrightarrow S_1$	0.22	0.03	0.19	0.69	0.70	0.01
	$S_1 \leftrightarrow S_2$	0.22	0.22	0.00	0.22	0.22	0.00
	$S_3 \leftrightarrow S_4$	0.10	0.02	0.08	0.50	0.63	0.13
	$S_4 \leftrightarrow S_5$	0.26	0.15	0.11	0.26	0.15	0.11
kink	$K_0 \leftrightarrow K_1$	0.44	0.45	0.01	0.21	0.17	0.04
	$K_0 \leftrightarrow K_2$	0.72	0.91	0.19	0.01	0.02	0.01
	$K_4 \leftrightarrow K_5$	0.47	0.46	0.01	0.25	0.12	0.13
	$K_4 \leftrightarrow K_6$	0.72	0.92	0.20	0.01	0.01	0.00
inner-corner	$IC_0 \leftrightarrow IC_1$	0.43	0.63	0.20	0.21	0.10	0.11
	$IC_2 \leftrightarrow IC_3$	0.46	0.62	0.16	0.25	0.08	0.17
outer-corner	$OC_0 \leftrightarrow OC_1$	0.30	0.29	0.01	0.32	0.22	0.10
	$OC_0 \leftrightarrow OC_1$ (Ex.)	0.51	0.41	0.10	0.52	0.33	0.19
	$OC_2 \leftrightarrow OC_5$ (Ex.)	0.37	0.32	0.05	0.37	0.32	0.05
	$OC_6 \leftrightarrow OC_8$ (Ex.)	0.24	0.16	0.08	0.24	0.16	0.08
step-down	$E_0 \leftrightarrow E_1$	0.27	0.09	0.18	0.72	0.75	0.03
	$E_0 \leftrightarrow E_1$ (Ex.)	0.31	0.01	0.30	0.77	0.67	0.10
	$E_2 \leftrightarrow E_3$	0.27	0.16	0.11	0.73	0.70	0.03
	$E_2 \leftrightarrow E_3$ (Ex.)	0.13	0.02	0.11	0.59	0.56	0.03

Mg diffusion processes on Mg$(10\bar{1}1)$

A detailed comparison of the activation energy results calculated with ReaxFF and DFT is provided in Table S2. On Mg$(10\bar{1}1)$, the dimer and trimer processes within a channel ($d_0 \leftrightarrow d_1$, $t_0 \leftrightarrow t_1$) are well reproduced by the force field (Figure S5). In contrast to DFT, however, two separated monomers are calculated to be thermodynamically more stable than the dimer in the $d_2 \leftrightarrow d_3$ process. A similar trend is calculated for the trimers. In DFT, a linear trimer structure is the most thermodynamically stable; with the force field, a triangular trimer with the third atom at position t_5 is preferred. Nevertheless, all trimer barriers are reproduced in ReaxFF with a maximum deviation of $\Delta|E_a| = 0.11\,\mathrm{eV}$.

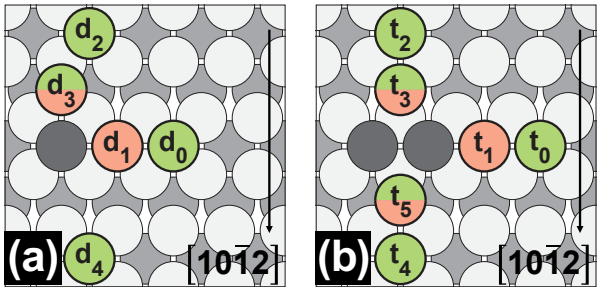

Figure S5: Overview and schematic representation of trained self-diffusion processes on Mg$(10\bar{1}1)$: a) Dimer, b) Trimer. Green atoms mark the initial, while red atoms mark the final position. Adapted from Ref. [1] Copyright (2022), with permission from Wiley-VCH.

Table S2: Comparison of activation energies E_a in eV calculated with ReaxFF and DFT using Equation (8) for forward and backward self-diffusion processes on Mg$(10\bar{1}1)$. DFT reference activation energy values were adopted from Fiesinger et al.[1]

Mg$(10\bar{1}1)$	Pathway	$E^{\mathrm{for}}_{\mathrm{a,ReaxFF}}$	$E^{\mathrm{for}}_{\mathrm{a,DFT}}$	$\lvert\Delta E^{\mathrm{for}}_{\mathrm{a}}\rvert$	$E^{\mathrm{rev}}_{\mathrm{a,ReaxFF}}$	$E^{\mathrm{rev}}_{\mathrm{a,DFT}}$	$\lvert\Delta E^{\mathrm{rev}}_{\mathrm{a}}\rvert$
dimer	$d_0 \leftrightarrow d_1$	0.37	0.25	0.12	0.63	0.58	0.05
	$d_2 \leftrightarrow d_3$	0.20	0.19	0.01	0.22	0.13	0.09
	$d_3 \leftrightarrow d_1$	0.22	0.15	0.07	0.45	0.51	0.06
	$d_4 \leftrightarrow d_1$	0.39	0.37	0.02	0.64	0.67	0.03
trimer	$t_0 \leftrightarrow t_1$	0.37	0.26	0.11	0.62	0.58	0.04
	$t_2 \leftrightarrow t_3$	0.19	0.19	0.00	0.29	0.20	0.09
	$t_3 \leftrightarrow t_1$	0.32	0.27	0.05	0.46	0.54	0.08
	$t_4 \leftrightarrow t_5$	0.36	0.31	0.05	0.66	0.57	0.09
	$t_5 \leftrightarrow t_1$	0.33	0.24	0.09	0.27	0.28	0.01

O adsorption on Mg(0001), Mg$(10\bar{1}0)$A, and Mg$(10\bar{1}1)$

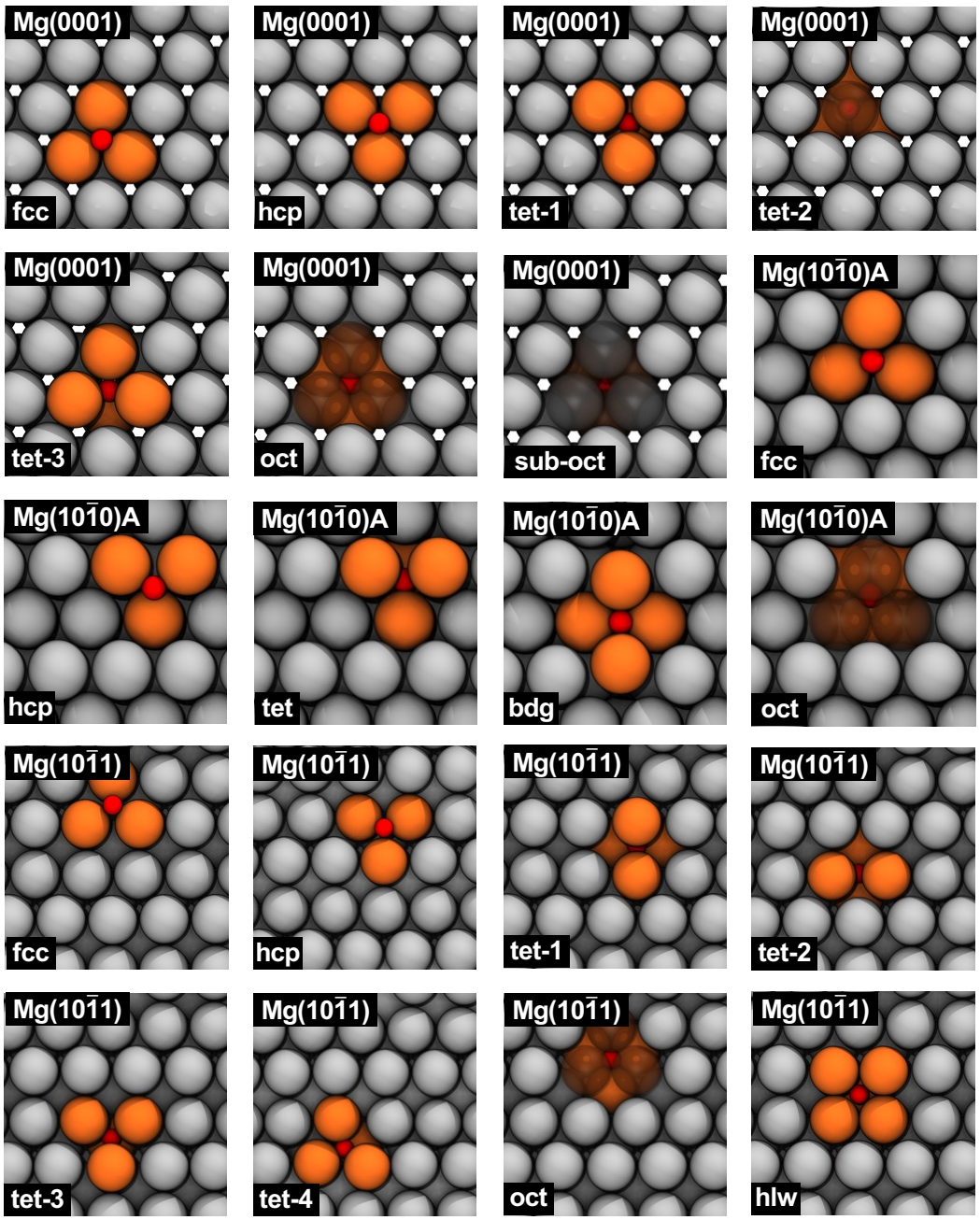

Figure S6: Schematic illustration of oxygen adsorption sites on on Mg(0001), Mg$(10\bar{1}0)$A, and Mg$(10\bar{1}1)$. The red-colored atom is the oxygen adsorbate, gray-colored atoms are surface atoms, and orange-colored atoms are surface atoms which coordinate to the oxygen adsorbate.

O diffusion processes on Mg(0001)

According to DFT, an oxygen atom diffuses on Mg(0001) (Table S3) in a zigzag route first from the fcc site by overcoming a barrier of 0.41 eV to the thermodynamically most stable tet-1 position (Figure S7c). From there, the oxygen atom moves to the oct position via the meta-stable tet-3 site with an activation energy of 0.72 eV. Finally, the oxygen atom overcomes 0.37 eV to reach the tet-2 position. In calculations with the trained force field, an oxygen atom adsorbed at the fcc position diffuses vertically down to the oct position overcoming a barrier of 0.20 eV (Figure S7a), or from the hcp to the tet-1 site overcoming 0.17 eV (Figure S7b), thereby underestimating the barrier by 50 % compared to DFT. The diffusion barriers within the surface are the same magnitude as the DFT barriers, with 0.54 eV from the tet-1 to the oct and 0.81 eV from the oct to the tet-2 site, respectively.

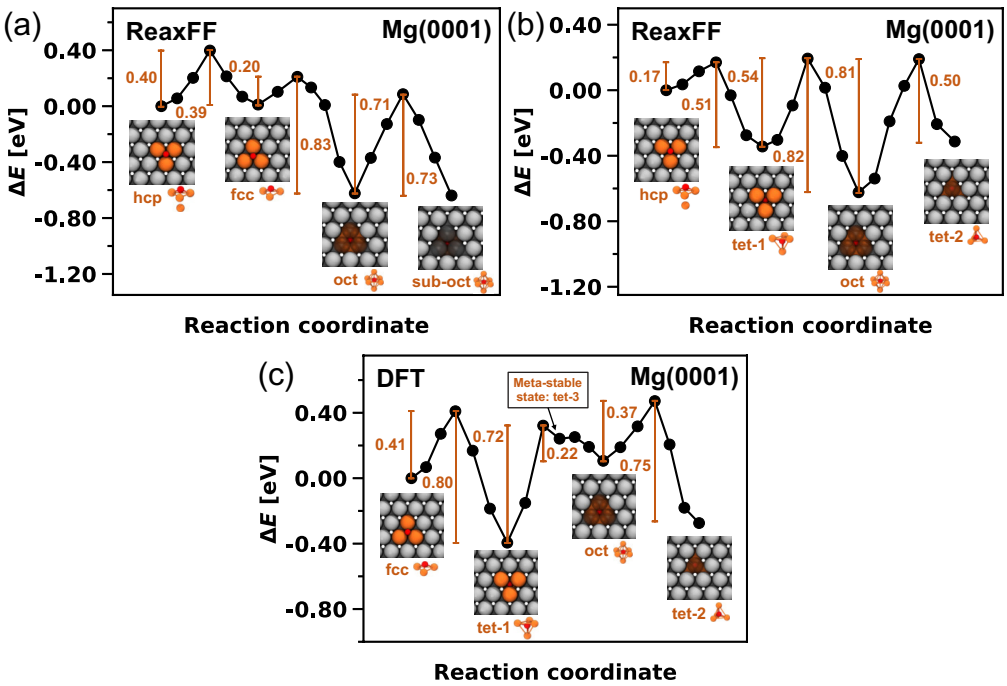

Figure S7: Diffusion profiles of an oxygen atom on Mg(0001) calculated with ReaxFF a) from the hcp to the fcc over the oct to the sub-oct site, b) from the hcp to the tet-1 over the oct to the tet-2 site, and with DFT c) from the fcc to the tet-1 over the oct to the tet-2 site.

O diffusion processes on Mg$(10\bar{1}0)$A

On Mg$(10\bar{1}0)$A (Table S4), oxygen atom diffusion as calculated with DFT is associated with only minor barriers of 0.12 eV/ 0.05 eV for diffusion between the bdg and the fcc sites (Figure S8c). With the trained force field, a barrier of 0.10 eV is calculated for diffusion between two fcc sites (Figure S8b). This result constitutes a significant deviation between DFT and the force field. While in DFT, the bdg position is stable, it corresponds to a transition state on the force field's potential energy surface. Similar to Mg(0001), the barrier from the oct to the

Table S3: Comparison of activation energies E_a in eV calculated using Equation (8) for forward and backward O-diffusion on Mg(0001) for ReaxFF and DFT.

Mg(0001)	$E^{for}_{a,ReaxFF}$	$E^{for}_{a,DFT}$	$E^{rev}_{a,ReaxFF}$	$E^{rev}_{a,DFT}$
hcp ↔ fcc	0.40	-	0.39	-
fcc ↔ oct	0.20	-	0.83	-
oct ↔ sub-oct	0.71	0.68	0.73	0.81
hcp ↔ tet-1	0.17	-	0.51	-
tet-1 ↔ oct	0.54	-	0.82	-
oct ↔ tet-2	0.81	0.37	0.50	0.75
fcc ↔ tet-1	-	0.41	-	0.80
tet-1 ↔ tet-3	-	0.72	-	0.08
tet-3 ↔ oct	-	0.01	-	0.15

tet position (0.72 eV) is higher than in the reverse direction (0.56 eV) calculated with the force field, while in DFT, the sequence is reversed (0.41 eV and 0.74 eV). For the force field, the low barrier of (0.05 eV) for diffusion from the hcp to the tet position, located below the first surface layer (Figure S8a), constitutes another deviation. In DFT, we calculated no barrier, causing the oxygen to relax directly to the tet position.

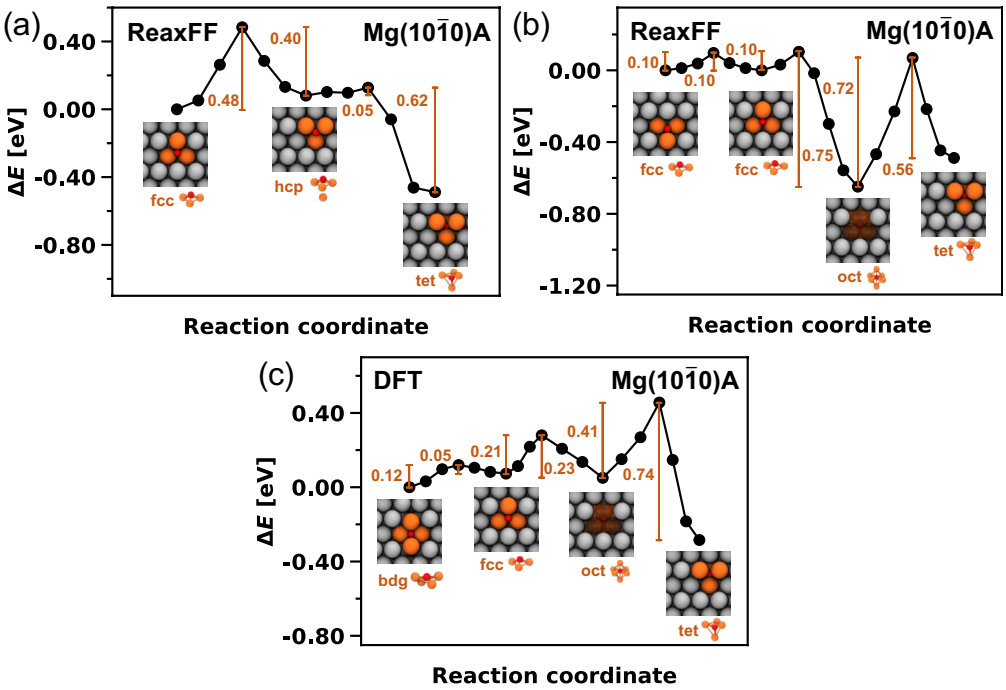

Figure S8: Diffusion profiles of an oxygen atom on Mg(10$\bar{1}$0)A calculated with ReaxFF a) from the fcc over the hcp to the tet site, b) from one fcc to the next fcc over the oct to the tet site, and with DFT c) from the bdg to the fcc over the oct to the tet site.

Table S4: Comparison of activation energies E_a in eV calculated using Equation (8) for forward and backward O-diffusion on Mg($10\bar{1}0$) for ReaxFF and DFT.

Mg($10\bar{1}0$)	$E^{\text{for}}_{\text{a,ReaxFF}}$	$E^{\text{for}}_{\text{a,DFT}}$	$E^{\text{rev}}_{\text{a,ReaxFF}}$	$E^{\text{rev}}_{\text{a,DFT}}$
fcc ↔ hcp	0.48	-	0.40	-
hcp ↔ tet	0.05	-	0.62	-
fcc ↔ fcc	0.10	-	0.10	-
bdg ↔ fcc	-	0.12	-	0.05
fcc ↔ oct	0.10	0.21	0.75	0.23
oct ↔ tet	0.72	0.41	0.56	0.74

O diffusion processes on Mg($10\bar{1}1$)

The oxygen atom diffusion barriers on Mg($10\bar{1}1$) are in agreement with the DFT reference activation energy (Table S5). E.g., the diffusion path from the hlw position via the tet-2 site (0.59 eV *vs.* 0.54 eV) to the tet-3 site (0.16 eV *vs.* 0.05 eV), as well as the reverse direction (0.25 eV *vs.* 0.19 eV for tet-3 to tet-2 and 0.51 eV *vs.* 0.49 eV for tet-2 to hlw), is accurately reproduced by the force field (cf. Figure S9b and S9d). However, differences emerge due to the overestimated thermodynamic stability of the oct position calculated by the force field. The diffusion of an oxygen atom from the tet-3 site (0.45 eV) or from the fcc to the oct site (0.13 eV) is highly preferred over its counterpart when calculations are performed with the force field (0.62 eV and 0.82 eV). In DFT, this sequence is reversed, and low barriers are associated with diffusion from the oct to the tet-3 site (0.16 eV) or the fcc position (0.11 eV). Equally of interest is the diffusion pathway for an oxygen atom at the hlw position coordinated by five Mg atoms towards the fcc or oct sites. While in the DFT, the oxygen atom significantly prefers to diffuse to the fcc position (0.66 eV), the trained force field predicts diffusion to the oct position (0.66 eV) (cf. Figure S9a and S9c).

Table S5: Comparison of activation energies E_a in eV calculated using Equation (8) for forward and backward O-diffusion on Mg($10\bar{1}1$) for ReaxFF and DFT.

Mg($10\bar{1}1$)	$E^{\text{for}}_{\text{a,ReaxFF}}$	$E^{\text{for}}_{\text{a,DFT}}$	$E^{\text{rev}}_{\text{a,ReaxFF}}$	$E^{\text{rev}}_{\text{a,DFT}}$
fcc ↔ oct	0.10	0.38	0.82	0.11
oct ↔ hlw	0.84	-	0.66	-
hlw ↔ tet-1	0.53	0.42	0.54	0.48
fcc ↔ hlw	-	0.62	-	0.66
hlw ↔ tet-2	0.59	0.54	0.51	0.49
tet-2 ↔ tet-3	0.16	0.05	0.25	0.19
tet-3 ↔ oct	0.45	-	0.62	-
tet-3 ↔ tet-4	-	0.56	-	0.12
tet-4 ↔ oct	-	0.07	-	0.11

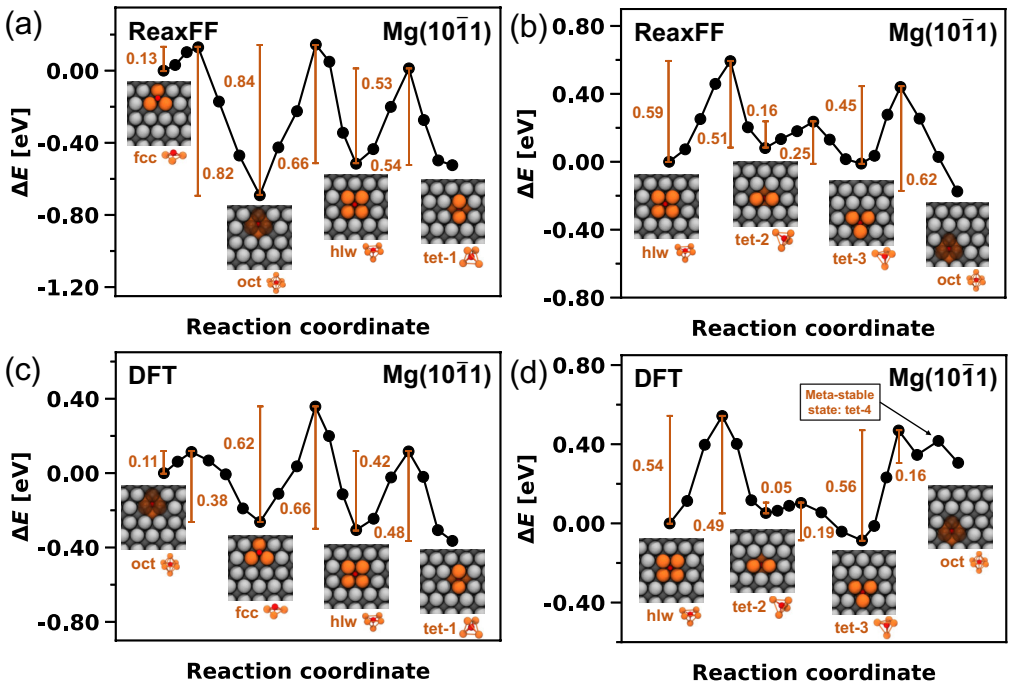

Figure S9: Diffusion profiles of an oxygen atom on Mg(10$\bar{1}$1) calculated with ReaxFF a) from the fcc to the oct over the hlw to the tet-1 site and b) from the hlw to the tet-2 over the tet-3 to the oct site and with DFT c) from the oct to the fcc over the hlw to the tet-1 site and d) from hlw to the tet-2 over the tet-3 to the oct site.

Grand-canonical Monte Carlo simulations of the oxidation of a magnesium nanoparticle

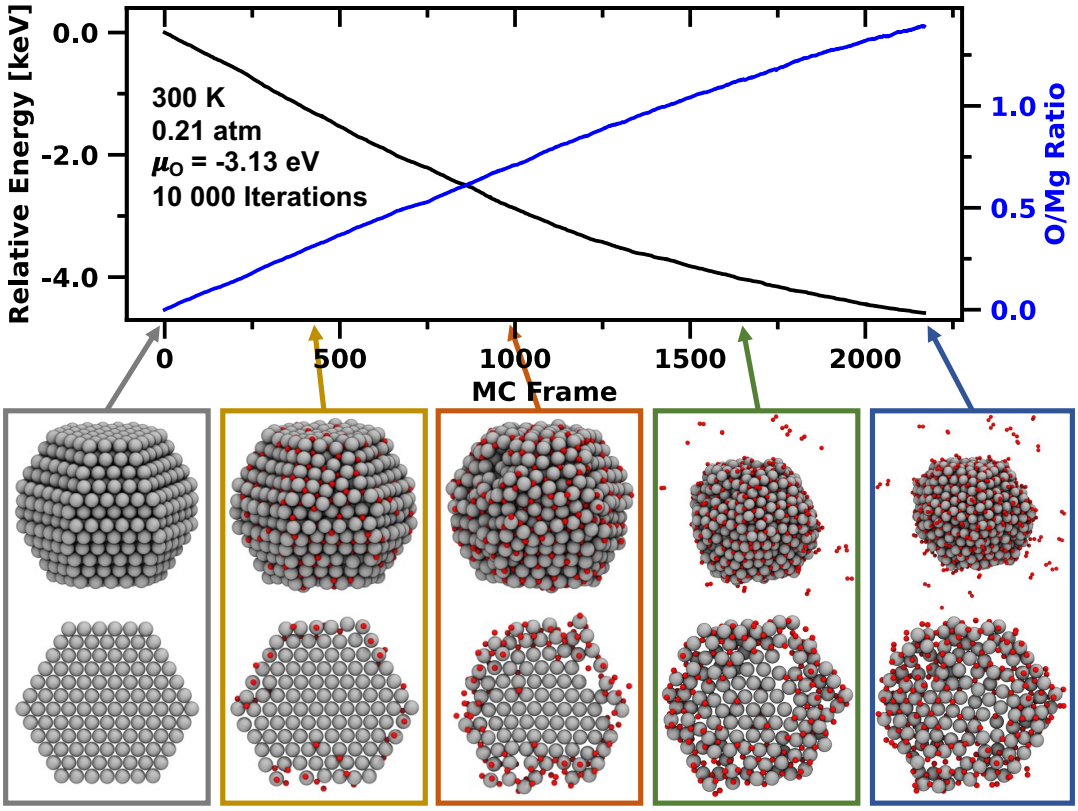

Figure S10: Grand-canonical Monte Carlo simulation showing the oxidation of an equilibrium-shaped Mg_{978} nanoparticle at 300 K and 0.21 atm. Initially, oxidation occurs at the surface but does not penetrate the particle's core. Instead, oxygen molecules are formed in the gas phase.

Molecular dynamics simulation of the passivation of the magnesium anode

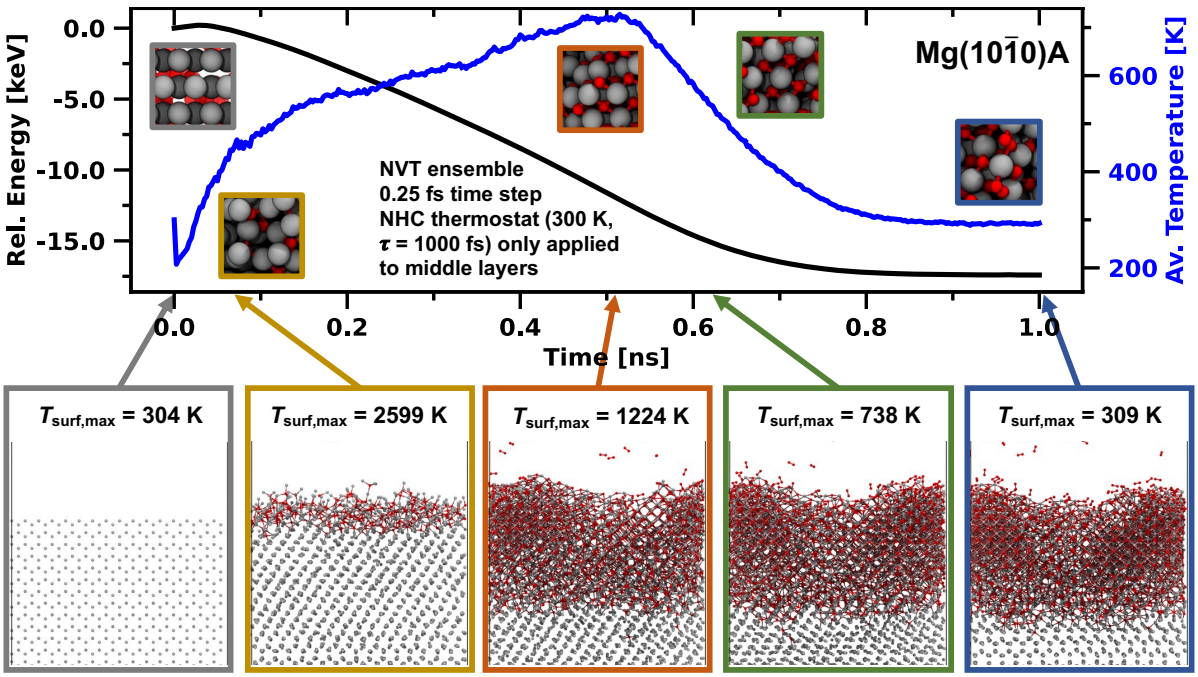

Figure S11: NVT simulation showing the oxidation behavior of Mg(10$\bar{1}$0)A at 300 K at 10 atm O_2 pressure. Upon contact of the first O_2 molecules, the surface heats up to several 1000 K. The high temperature fosters the formation of an rocksalt interphase on top of the Mg anode. The maximum surface temperature $T_{\mathrm{surf,max}}$ was determined from the temperature profiles in Figure S15.

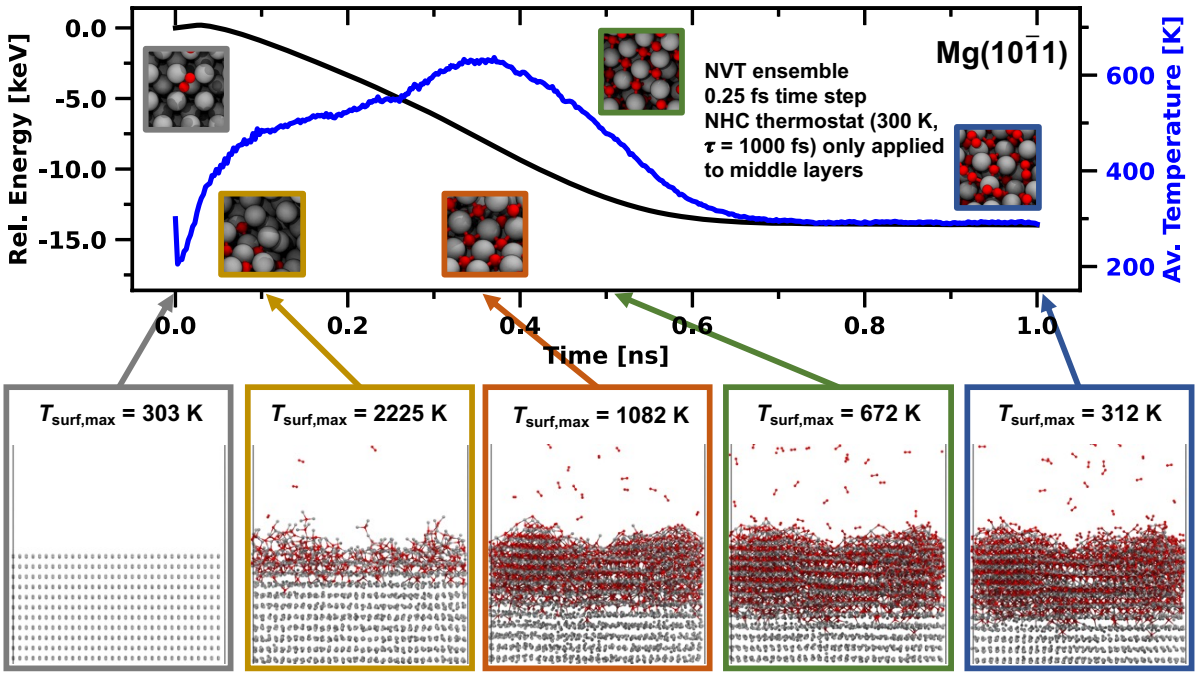

Figure S12: NVT simulation showing the oxidation behavior of Mg(10$\bar{1}$1) at 300 K at 10 atm O_2 pressure. Upon contact of the first O_2 molecules, the surface heats up to several 1000 K. The high temperature fosters the formation of an rocksalt interphase on top of the Mg anode. The maximum surface temperature $T_{\mathrm{surf,max}}$ was determined from the temperature profiles in Figure S16.

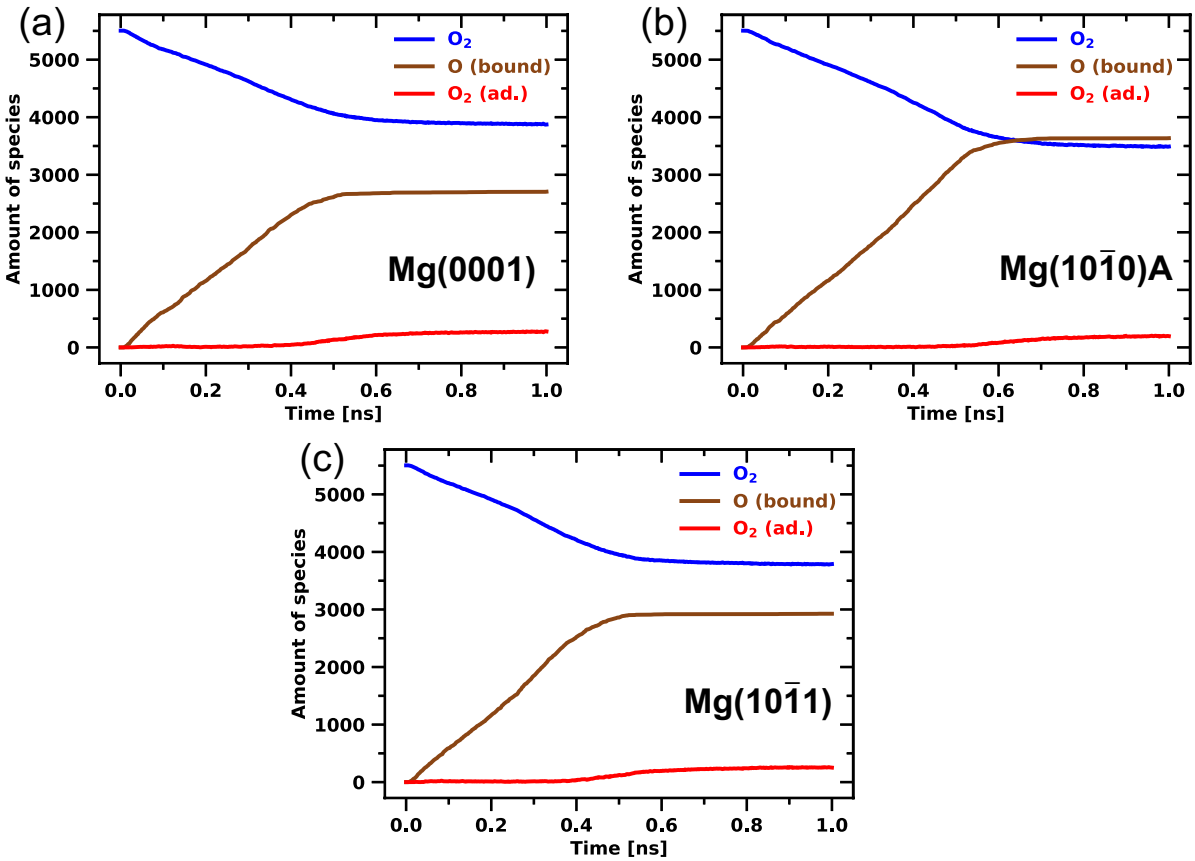

Figure S13: Analysis of the composition of molecular oxygen in the atmosphere O_2, adsorbed oxygen on the Mg surface O_2 (ad.), and bound oxygen atoms in the Mg bulk O (bound) for the NVT calculations on (a) Mg(0001), (b) Mg(10$\bar{1}$0)A, and (c) Mg(10$\bar{1}$1). Oxygen was counted as being in the atmosphere when two oxygen atoms were closer than 1.5 Å, but both were more than 2.45 Å away from a Mg bulk atom; they were considered adsorbed if two oxygen atoms were closer than 1.5 Å and one was closer than 2.45 Å from a Mg bulk atom or bound if one oxygen atom was closer than 2.45 Å to a Mg bulk atom but farther than 2.45 Å from the nearest oxygen atom.

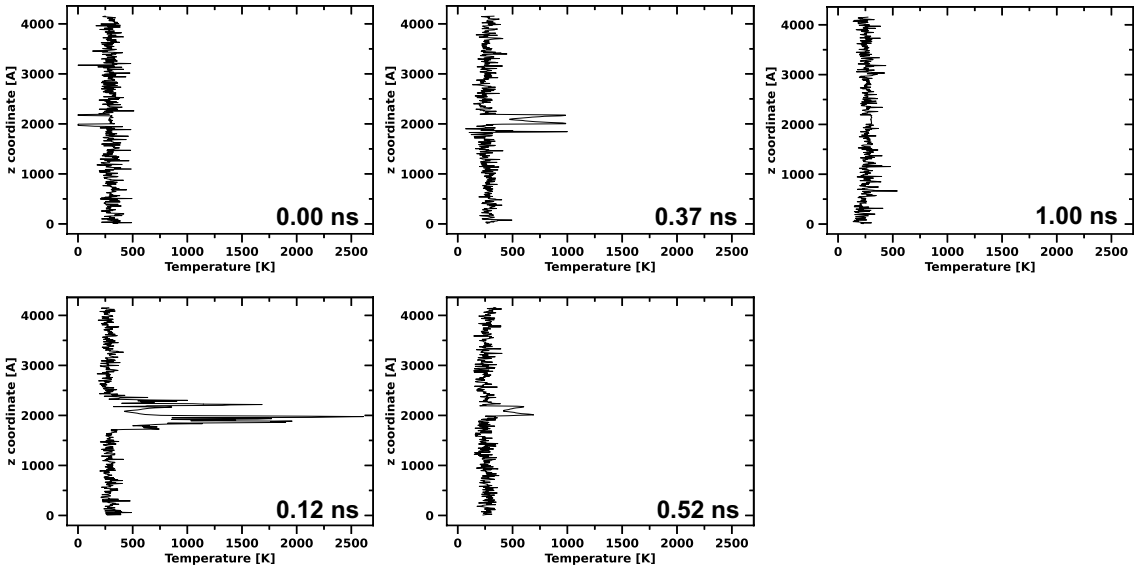

Figure S14: Temperature profiles along the z-axis from the selected snapshots in the colored boxes from the NVT calculation on Mg(0001) in Figure 7. The z-axis was divided into 500 equally sized sections, and the temperature of all atoms inside the corresponding box was calculated time-averaged over all MD steps since the previous snapshot. See documentation from SCM about Molecular Dynamics on https://www.scm.com/doc/AMS/Tasks/Molecular_Dynamics.html (accessed: August 2022).

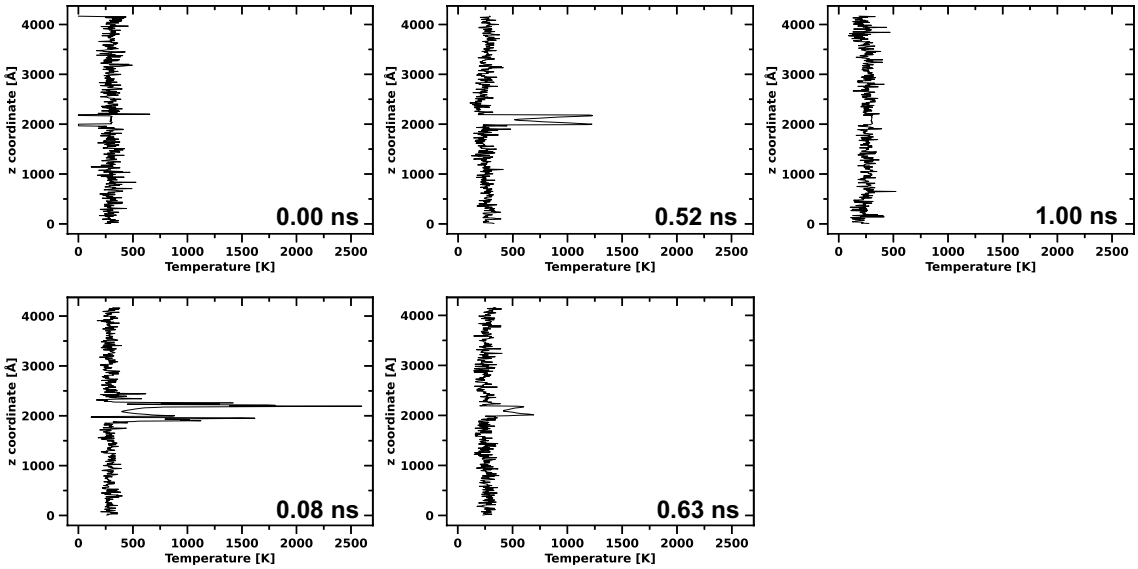

Figure S15: Temperature profiles along the z-axis from the selected snapshots in the colored boxes from the NVT calculation on Mg(10$\bar{1}$0)A in Figure S11. The z-axis was divided into 500 equally sized sections, and the temperature of all atoms inside the corresponding box was calculated time-averaged over all MD steps since the previous snapshot. See documentation from SCM about Molecular Dynamics on https://www.scm.com/doc/AMS/Tasks/Molecular_Dynamics.html (accessed: August 2022).

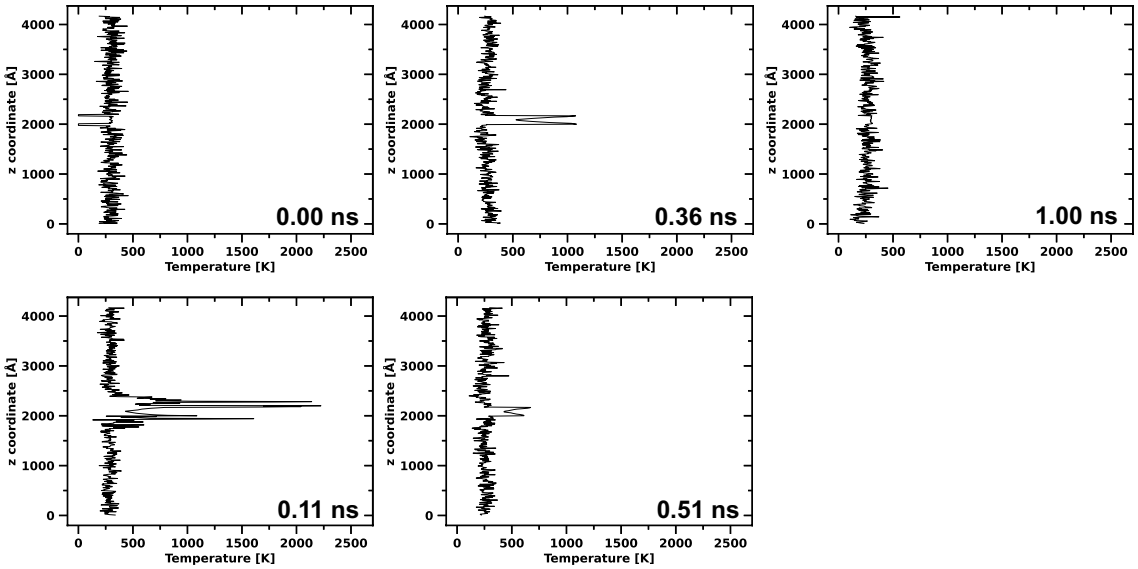

Figure S16: Temperature profiles along the z-axis from the selected snapshots in the colored boxes from the NVT calculation on Mg($10\bar{1}1$) in Figure S12. The z-axis was divided into 500 equally sized sections, and the temperature of all atoms inside the corresponding box was calculated time-averaged over all MD steps since the previous snapshot. See documentation from SCM about Molecular Dynamics on https://www.scm.com/doc/AMS/Tasks/Molecular_Dynamics.html (accessed: August 2022).

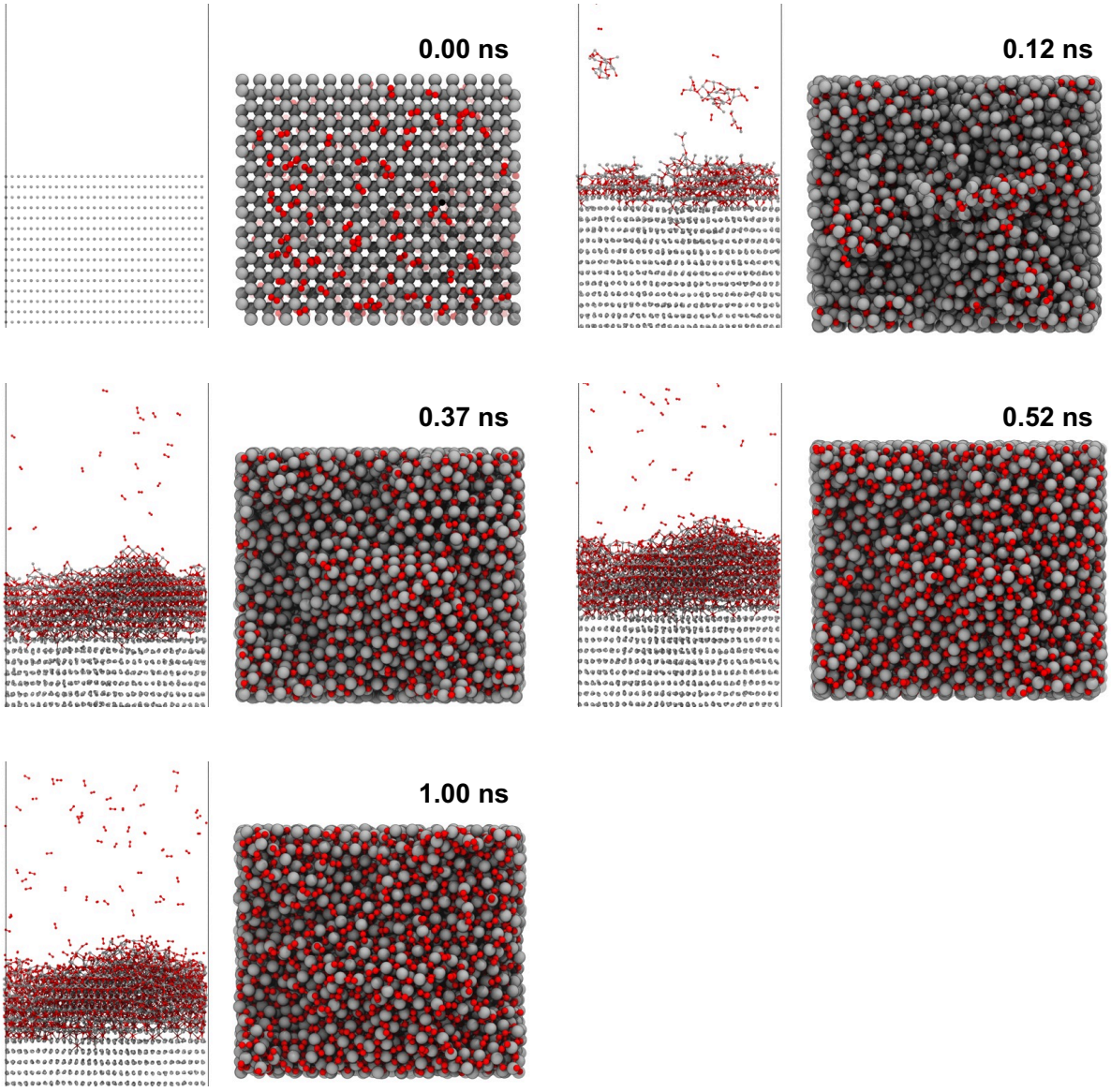

Figure S17: Enlarged images of the side and top views of the selected snapshots in the colored boxes from the NVT calculation on Mg(0001) in Figure 7.

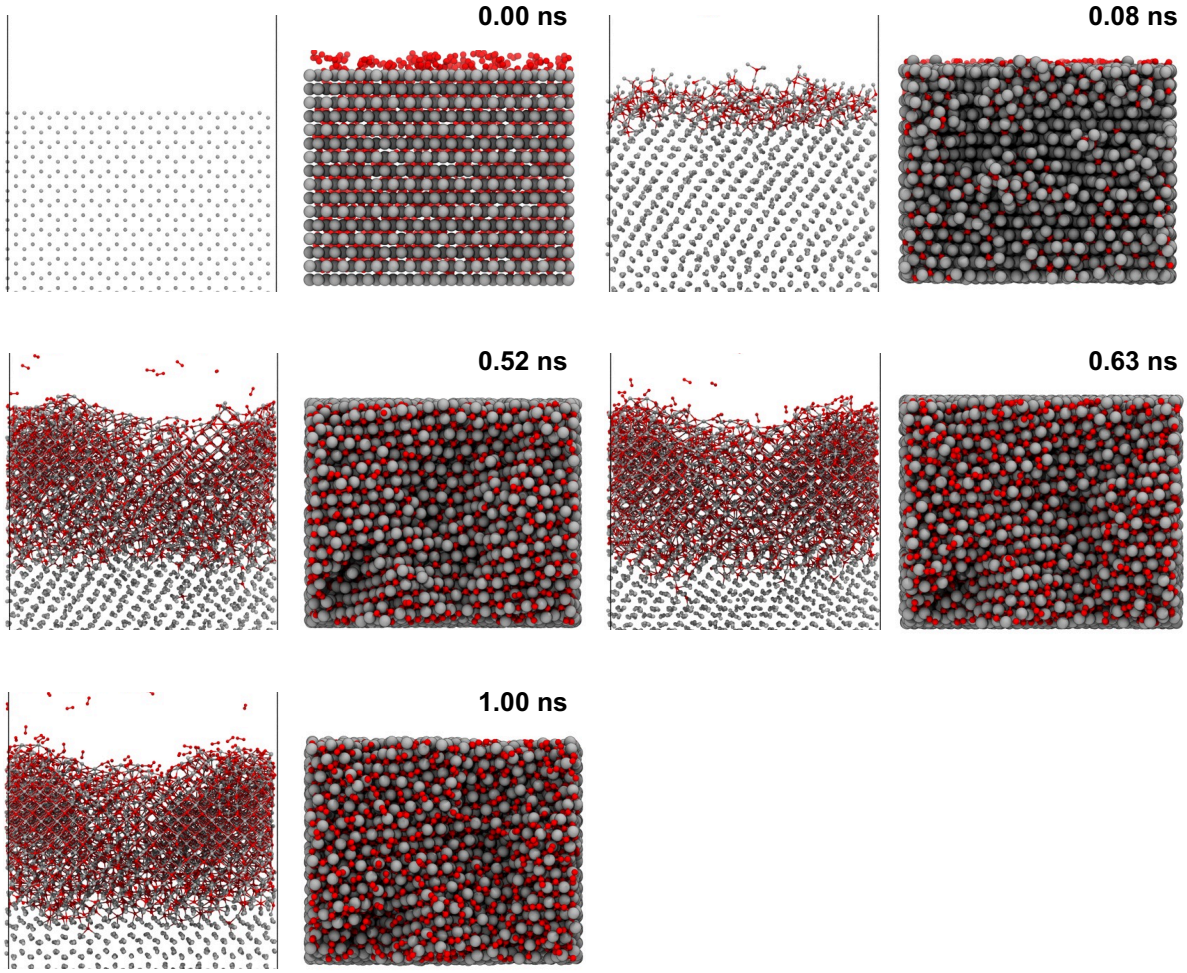

Figure S18: Enlarged images of the side and top views of the selected snapshots in the colored boxes from the NVT calculation on Mg(10$\bar{1}$0)A in Figure S11.

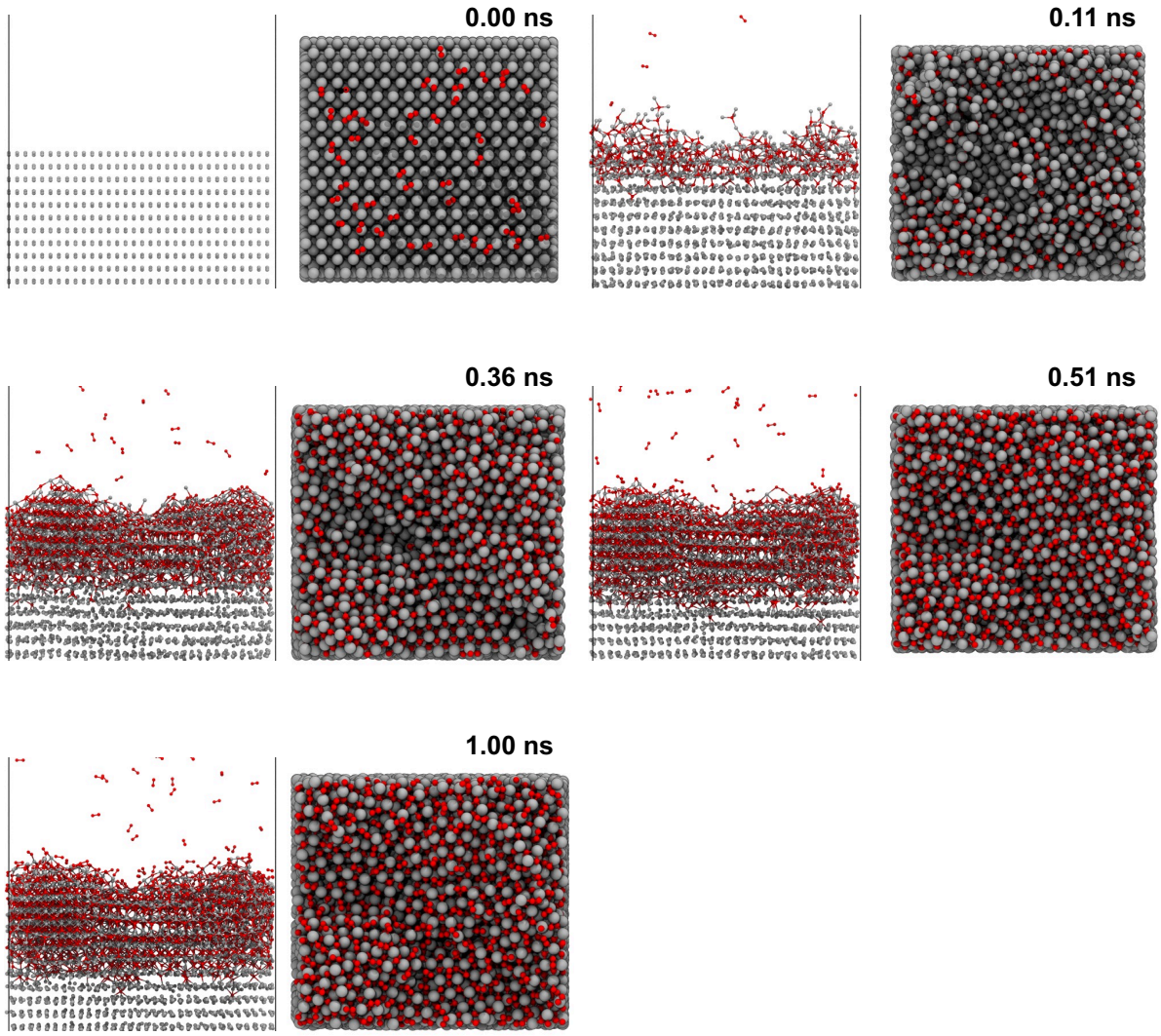

Figure S19: Enlarged images of the side and top views of the selected snapshots in the colored boxes from the NVT calculation on Mg($10\bar{1}1$) in Figure S12.

References

[1] F. Fiesinger, D. Gaissmaier, M. van den Borg, T. Jacob, *ChemSusChem* **2022**, *15*, e202200414.